Research Paper

Journal of Engineering and Technological Sciences

Defect-Engineered TiO_2 Photocatalysts for Enhanced Methylene Blue Degradation

Tri Partono Adhi[1,*], Galang Ananta Dwipayana[1], Dwiwahju Sasongko[1,2], I Gede Wenten[1], Hary Devianto[1,2], & Wibawa Hendra Saputera[1,2]

[1]Department of Chemical Engineering, Faculty of Industrial Technology, Institut Teknologi Bandung, Jalan Ganesa No. 10, Bandung 40132, Indonesia
[2]Research Center for New and Renewable Energy, Institut Teknologi Bandung, Jalan Ganesa No. 10, Bandung 40132, Indonesia, Indonesia

*Corresponding author: tpadhi@itb.ac.id

Abstract

Textile wastewater containing synthetic dyes is a significant environmental concern due to its high color intensity, toxicity, chemical stability, and resistance to conventional treatment. This work prepared Ti^{3+} self-doped TiO_2 photocatalysts using a simple sol-gel route combined with $NaBH_4$-assisted calcination. The strategy was designed to generate intrinsic lattice defects, mainly Ti^{3+} centers and oxygen vacancies, in anatase TiO_2 without the use of flammable reducing gases or complicated post-synthesis treatments. The influence of calcination temperature was examined by preparing samples at 200, 500, and 600 °C. XRD results showed that the selected samples maintained the anatase TiO_2 phase, indicating that the reduction-calcination treatment did not produce detectable secondary crystalline phases. Higher calcination temperature increased the degree of crystallinity, with crystallinity values of 59.1%, 68.2%, and 69.6% for the samples of T-200, T-500, and T-600, respectively. Raman spectra confirmed the anatase framework and revealed features related to lattice disorder in the reduced samples, while EPR analysis directly confirmed Ti^{3+}/oxygen-vacancy defect sites, with the strongest signal observed for T-600. UV-vis DRS demonstrated that the samples calcined at 500 and 600 °C absorbed more strongly in the visible region. The T-600 sample showed an effective band gap of 2.42 eV, evidencing that defect-related states contributed to broader light harvesting. Photocatalytic evaluation indicated that methylene blue degradation improved with increasing calcination temperature, and the best performance was obtained using T-600, with an apparent rate constant of 0.017 min^{-1}. Reusability testing showed that T-600 retained activity for three cycles, although the rate constant decreased to 0.0116 and 0.0089 min^{-1} in the second and third cycles, respectively. The enhanced activity is attributed to the combined contribution of higher anatase crystallinity, improved visible-light response, and an appropriate concentration of Ti^{3+}-oxygen vacancy sites that support charge separation and reactive oxygen species formation.

Keywords: *defect; methylene blue; oxygen vacancy; photocatalysis; TiO_2; wastewater.*

Introduction

As the global population and consumer demand continue to increase, textile production has expanded rapidly worldwide. The growth of the fashion, apparel, and household textile sectors has led to higher water consumption and greater wastewater generation from dyeing and finishing processes. Textile wastewater is a major environmental concern because it often contains synthetic dyes, salts, surfactants, and other auxiliary chemicals. Dyes are among the most problematic constituents because they possess high solubility, stable aromatic structures, strong coloration, chemical persistence, and possible toxicity. When released without sufficient treatment, colored wastewater can limit light penetration into water bodies, disturb photosynthetic processes, and endanger aquatic ecosystems as well as human health. Since many commercial dyes are poorly removed by conventional primary and secondary treatment, more effective tertiary treatment technologies are required (Shindhal et al., 2021).

Advanced oxidation processes (AOPs) are promising tertiary treatment technologies for dye-containing wastewater. Among various AOPs, heterogeneous photocatalysis is attractive because a semiconductor can be activated by light to produce reactive oxygen species that oxidize organic pollutants (Saputera et al., 2023). Highly oxidative species, especially hydroxyl and superoxide radicals, can break down complex dye molecules into smaller intermediates and may further convert them to CO_2 and H_2O (Deng & Zhao, 2015). Photocatalysis is also considered environmentally attractive

ISSN: 2337-5779
J. Eng. Technol. Sci. Vol. 58, No. 5, 2026, 732-744
DOI: 10.5614/j.eng.technol.sci.2026.58.5.10

DOI: 10.5614/j.eng.technol.sci.2026.58.5.10

because solar irradiation can potentially be used as the energy source (Saputera et al., 2024). TiO_2 remains one of the most intensively investigated photocatalysts owing to its availability, affordability, chemical robustness, and low toxicity. Nevertheless, pristine TiO_2 is constrained by a wide band gap of about 3.2 eV, which limits absorption mainly to ultraviolet light, and by rapid electron-hole recombination (C. Xu et al., 2014). Accordingly, TiO_2 modification is needed to expand light absorption, retard charge recombination, and improve pollutant interaction at the catalyst surface (Gao et al., 2019).

One effective approach to improve TiO_2 photocatalytic activity is defect engineering through the formation of Ti^{3+} species and oxygen vacancies, resulting in TiO_{2-x}. The introduction of Ti^{3+} centers and oxygen vacancies can produce TiO_{2-x}, in which defect-derived electronic states alter the optical and charge-transport properties. These sites may create intermediate energy levels, reduce the effective band gap, increase visible-light absorption, and prolong charge separation. Various approaches have been applied to generate Ti^{3+} and oxygen vacancies in TiO_2, including self-doped using Ti_2O_3 (Hamdy et al., 2014; Saputera et al., 2015), vacuum reduction (Guillemot et al., 2002), hydrogenation (Saputera et al., 2015), metal reduction (Lee et al., 2018), chemical reduction (Jiménez et al., 2023), and plasma treatment (Bharti et al., 2016). However, some of these methods require hazardous gases, high energy input, or complex operating conditions, which may limit their practicality for larger-scale applications. Thus, a simpler, safer, and more cost-effective synthesis route is needed.

In this study, Ti^{3+} self-doped TiO_2 photocatalysts were synthesized through a one-step calcination process using $NaBH_4$ as a reducing agent, adapted from Fang et al. (Fang et al., 2014). The synthesis also incorporated an HCl washing stage to remove boron-containing residues generated during reduction. Although $NaBH_4$-reduced TiO_2 has been previously reported, the novelty of this work lies in systematically clarifying how calcination temperature controls the balance between defect formation and anatase crystallinity in a $NaBH_4$-assisted sol-gel route. Specifically, this study correlates calcination-dependent changes in phase structure, crystallinity, Raman features, visible-light absorption, morphology, and methylene blue degradation kinetics. This route was selected because it uses readily available chemicals and can be performed at atmospheric pressure, in air, and at moderate calcination temperatures, without H_2, Ar, He, or other reducing atmospheres.

Materials and Methods

Materials

Titanium Butoxide (≥ 99.5%, Sigma-Aldrich), 0.6 M Nitric Acid (A.R., Merck), Ethanol (A.R., Merk), sodium Borohydride (≥ 99%, Sigma-Aldrich), Methylene Blue (A.R., Merck) and 1 M Hydrochloric Acid (A.R., Merck) were used without further purification.

Photocatalyst Synthesis

The defective TiO_2 photocatalysts were prepared by a $NaBH_4$-assisted calcination procedure adapted from Fang et al. (Fang et al., 2014). Solution A was obtained by dissolving 5 mL of titanium butoxide in 25 mL of ethanol. In a separate vessel, solution B was prepared from 4 mL of 0.6 M HNO_3 and 5 mL of ethanol. Solution B was introduced dropwise into solution A while the mixture was continuously stirred, producing a uniform sol. Afterward, 0.1 g of $NaBH_4$ was added as the reducing agent, which induced gel formation. The gel was placed in a ceramic crucible and calcined in air at 200, 500, or 600 °C for 180 min. Calcination was capped at 600 °C to maintain the anatase TiO_2 phase, as higher temperatures of 700-800 °C can promote anatase-to-rutile transformation and particle sintering, potentially reducing surface area and altering Ti^{3+}/oxygen-vacancy defects (Saputera et al., 2015). Thus, 600 °C was selected to improve crystallinity while preserving the anatase framework, consistent with previous reports on Ti^{3+}-containing titania photocatalysts (Hamdy et al., 2014). The reduced samples were named T-XXX, where XXX denotes the calcination temperature; thus, T-200, T-500, and T-600 represent the samples calcined at 200, 500, and 600 °C, respectively. A reference TiO_2 sample was synthesized under the same conditions without $NaBH_4$ addition and calcined at 500 and 600 °C; these samples were denoted as T-500-N and T-600-N. After calcination, 0.5 g of each TiO_2 powder was treated in 100 mL of 1 M HCl for 6 h under stirring to dissolve residual boron-based species. The solids were then repeatedly rinsed with distilled water and dried under vacuum at 60 °C for 12 h to obtain the final Ti^{3+} self-doped TiO_2 photocatalysts.

Physicochemical Characterizations

The synthesized photocatalysts were examined by XRD, Raman spectroscopy, UV-vis DRS, and SEM. XRD measurements were carried out at room temperature using a Bruker D8 Advance diffractometer with Cu-Kalpha radiation (λ = 0.15406 nm) over a 2θ range of 20-80°. The diffractograms were used to identify the crystalline phase and to estimate crystallinity and crystallite size. The mean crystallite size was calculated using the Scherrer equation. Raman spectra were recorded on a Bruker Raman Senterra spectrometer with a 532 nm excitation laser to verify the TiO_2 phase and probe lattice disorder related to Ti^{3+} and oxygen vacancy formation. Optical absorption was investigated using a Thermo UV-vis spectrophotometer operated in diffuse reflectance mode, with $BaSO_4$ as the reference and a spectral range of 200-800 nm. The reflectance data were further used to evaluate the absorption response and band gap energy. Surface morphology was observed by SEM using a Hitachi SU3500 instrument. Defect characteristics were examined by electron paramagnetic resonance (EPR) spectroscopy using a Bruker ELEXSYS E-500 instrument (Billerica, MA, USA). The spectra were recorded in the X-band region at a frequency of 9.419 GHz. During the analysis, the microwave power, modulation amplitude, and measurement temperature were maintained at 2 mW, 5 G, and 120 K, respectively.

Photocatalytic Assessment

Click or tap here to enter text.Photocatalytic activity was tested through methylene blue degradation under simulated solar irradiation using the reactor configuration shown in Figure 1, following the approach of Saputera, et al. (Saputera et al., 2021). In each run, 0.2 g of photocatalyst was suspended in 200 mL of 10 ppm methylene blue solution in a 500 mL quartz reactor. The suspension was sonicated for 15 min to obtain a well-dispersed mixture. Before illumination, the system was stirred in the dark for 30 min to reach adsorption-desorption equilibrium between methylene blue and the catalyst surface. The reaction was then started by switching on a 300 W Xe lamp with an emission range of 200-1000 nm. No optical filter was used in this study, therefore, the photocatalytic test was conducted under the full Xe lamp spectrum, including both UV and visible-light regions. Oxygen was continuously bubbled through the suspension at 150 mL/min to assist reactive oxygen species generation. The reaction was continued for 180 min under near-room-temperature conditions maintained by a water-cooling system. Every 30 min after irradiation started, 5 mL of suspension was collected and centrifuged to separate the photocatalyst. The remaining methylene blue concentration was determined by UV-vis spectrophotometry at its maximum absorption wavelength, and degradation performance was evaluated from the change in concentration with irradiation time.

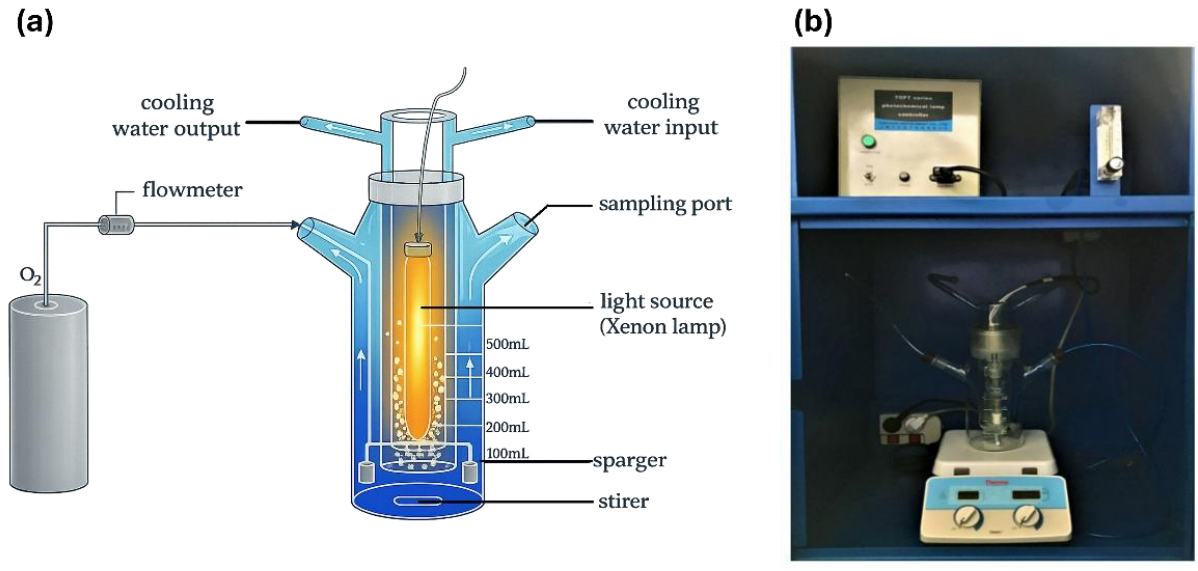

Figure 1 Photocatalytic reactor configuration: (a) schematic representation and (b) laboratory setup used for methylene blue degradation under Xe lamp irraditation.

Results

Photocatalysts Synthesis

A total of six TiO_2 samples were synthesized to evaluate the effect of $NaBH_4$ reduction and calcination temperature on defect formation. Five samples were prepared using $NaBH_4$ as the reducing agent and calcined at 200, 500, and 600 °C, denoted as T-200, T-500, and T-600, respectively. For comparison, a non-reduced TiO_2 sample was synthesized without

DOI: 10.5614/j.eng.technol.sci.2026.58.5.10

$NaBH_4$ and calcined at 500 °C, denoted as T-500-N. Figure 2 shows that the sample color changed significantly depending on the reduction treatment and calcination temperature. T-200 and T-500-N appeared white, suggesting a relatively low concentration of defect sites. Although $NaBH_4$ was added to T-200, the low calcination temperature likely provided insufficient thermal energy to form a substantial amount of Ti^{3+} and oxygen vacancies. In comparison, the reduced samples treated at higher temperatures became darker, with T-500 appearing black and T-600 appearing dark brown. This visual change suggests stronger absorption in the visible region and is typically linked to Ti^{3+}-oxygen vacancy defects in reduced TiO_2 (Ullattil & Ramakrishnan, 2018). However, T-600 was slightly lighter than T-500, indicating that the relationship between calcination temperature and defect concentration may not be fully linear. At higher temperatures, partial reoxidation or structural rearrangement may reduce certain defect states, resulting in a lighter color. The brown and gray-black colors observed here agree with previous reports on $NaBH_4$-reduced TiO_2 materials (Ren et al., 2015). Thus, the powder appearance provides an initial indication that $NaBH_4$ and calcination temperature modify the optical and defect-related properties of TiO_2.

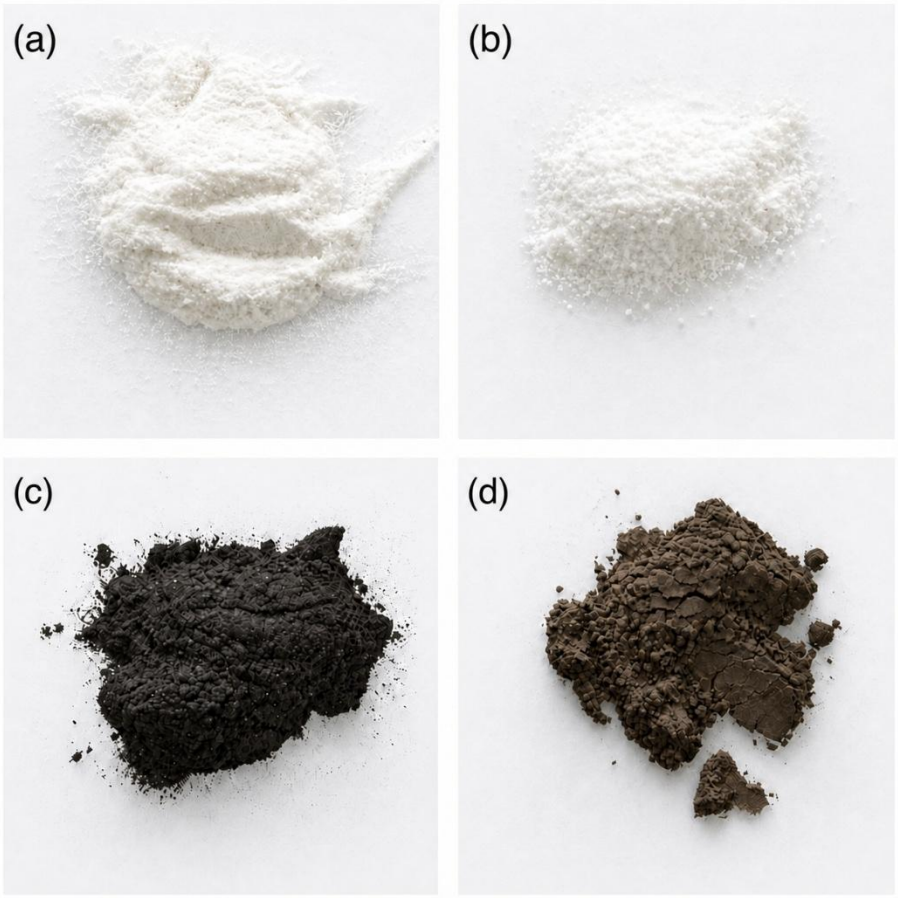

Figure 2 Photographs of the synthesized TiO_2 powders: (a) T-200, (b) T-500-N, (c) T-500, and (d) T-600.

Physicochemical Characterizations

Figure 3(a) presents the XRD patterns of T-200, T-500, and T-600. The diffraction peaks located 2θ values of 25.3°, 37.8°, 48.0°, 53.9°, 55.1°, 62.7°, 68.8°, 70.3°, and 75.0° can be assigned to the (101), (004), (200), (105), (211), (204), (116), (220), and (215) planes of anatase TiO2, respectively, based on JCPDS no. 21-1272. No additional peaks related to rutile, brookite, or crystalline impurities were observed, confirming that the synthesized samples retained a pure anatase phase after $NaBH_4$-assisted reduction and calcination. The diffraction peaks became more intense as calcination temperature increased, showing an improvement in crystallinity. The crystallinity values were 59.1%, 68.2%, and 69.6% for T-200, T-500, and T-600, respectively. The crystallite size followed the same tendency, increasing from 4.22 nm for T-200 to 5.63 nm for T-500 and 8.77 nm for T-600, which indicates thermally driven crystal growth during calcination. $NaBH_4$ reduction may generate boron-containing residues such as $NaBO_2$, $Na_2B_4O_7{\cdot}5H_2O$, $Na_{0.23}TiO_2$, $Na_3B_3O_6$, and B_2O_3 on the material surface (Fang et al., 2014). However, no characteristic diffraction peaks associated with these species were detected within the measured 2θ range, suggesting that the HCl washing step effectively removed residual boron-based compounds.

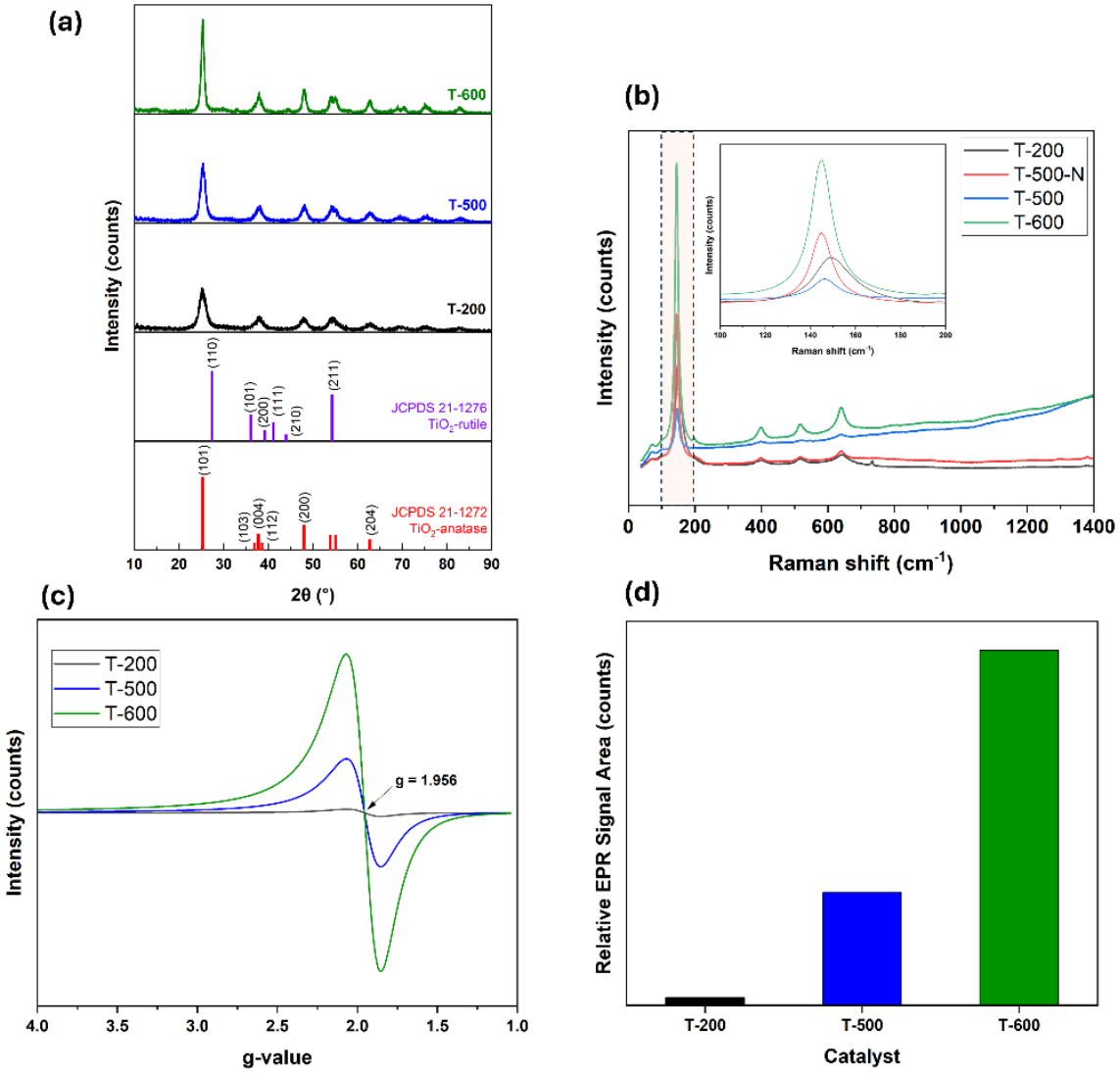

Figure 3 Structural and defect characterization of TiO_2 samples calcined at different temperatures: (a) XRD patterns with the reference anatase and rutile phase of TiO_2 pattern based on JCPDS No. 21-1272 and No. 21-1276, (b) Raman spectra, (c) EPR spectra, and (d) relative EPR signal area.

The Raman spectra of T-200, T-500-N, T-500, and T-600 are presented in Figure 3(b). The characteristic Raman bands appeared at approximately 144 cm^{-1} (E_g), 197 cm^{-1} (E_g), 396 cm^{-1} (B_{1g}), 515 cm^{-1} (A_{1g}), and 639 cm^{-1} (E_g), which are consistent with the vibrational modes of anatase TiO_2. These results further confirm the anatase phase, in agreement with the XRD analysis. Among the samples, T-500 showed markedly lower Raman peak intensity. This feature may be associated with the presence of defect sites, although Raman spectroscopy alone cannot precisely identify the specific type of defect (Abdullah et al., 2020). The Raman peak intensity is influenced by several factors, including calcination temperature, crystallite size, phase composition, defect concentration, and morphology. In general, higher calcination temperatures can increase Raman intensity due to improved crystallinity and crystal growth, as reported in previous studies. This trend was observed for most samples, except T-500, which showed significantly lower intensity. The reduced intensity of T-500 may be related to differences in particle size distribution, morphology, or a higher concentration of defect sites such as oxygen vacancies and Ti^{3+} species. The anomalous behavior of T-500 suggests that defect formation may compete with crystallinity improvement, depending on the synthesis route and $NaBH_4$ incorporation during gel formation (Fang et al., 2014). In contrast, T-600 exhibited the highest Raman intensity mainly because calcination at 600 °C improved anatase crystallinity and promoted crystal growth, as also supported by the XRD results. At the same time, UV-vis DRS confirmed that T-600 still retained sufficient defect-related visible-light absorption. Thus, the superior photocatalytic performance of T-600 is attributed to an optimized balance between anatase crystallinity and Ti^{3+}/oxygen-vacancy defect states (Zywitzki et al., 2017).

Peak broadening and shifting in the Raman bands, particularly at 144, 396, 515, and 639 cm^{-1}, can indicate lattice disorder associated with oxygen vacancies and Ti^{3+} defects. The 144 cm^{-1} band of T-200 showed the largest full width at half maximum and peak shift, while T-500 exhibited a slight shift compared with T-500-N. For the 396 cm^{-1} band, T-500-

DOI: 10.5614/j.eng.technol.sci.2026.58.5.10

N showed the highest wavenumber and broadening, whereas T-500 displayed notable broadening. At 515 and 639 cm^{-1}, T-500 showed the most pronounced peak shift and broadening among the samples. These observations indicate that defect-related lattice distortion occurred in the synthesized TiO_2 samples (Zywitzki et al., 2017). However, the changes in peak position and broadening did not show a clear monotonic relationship with calcination temperature. Therefore, although Raman analysis suggests the presence of defects, the correlation between calcination temperature and oxygen vacancy or Ti^{3+} formation remains inconclusive based solely on Raman spectra.

To further evaluate the defect concentration, EPR characterization was performed on T-200, T-500, and T-600. As shown in Figure 3(c), all samples exhibited an EPR signal at around g = 1.956, which can be assigned to Ti^{3+} species and oxygen-vacancy-related defect sites in TiO_2. The signal intensity increased markedly with increasing calcination temperature, with T-600 showing the strongest response. The relative EPR signal area in Figure 3(d) further confirms that T-600 possessed the highest defect concentration, followed by T-500 and T-200. This indicates that the combined $NaBH_4$ treatment and higher calcination temperature effectively promoted the formation of Ti^{3+}/oxygen-vacancy defect sites.

The UV-vis DRS results for T-200, T-500-N, T-500, and T-600 are provided in Figure 4(a). All catalysts absorbed strongly in the ultraviolet region, as expected for TiO_2. In addition, the reduced samples T-500 and T-600 displayed stronger absorption in the visible region, with T-500 showing the most intense visible-light response. This enhancement is attributed to defect states generated by $NaBH_4$-assisted reduction, particularly oxygen vacancies and Ti^{3+} centers. The optical behavior is consistent with the Raman observations, in which T-500 showed reduced Raman intensity and stronger background features associated with disorder. The DRS results also explain the powder colors: T-200 and T-500-N remained white because their visible absorption was weak, whereas T-500 and T-600 became black and dark brown due to increased absorption across the visible range.

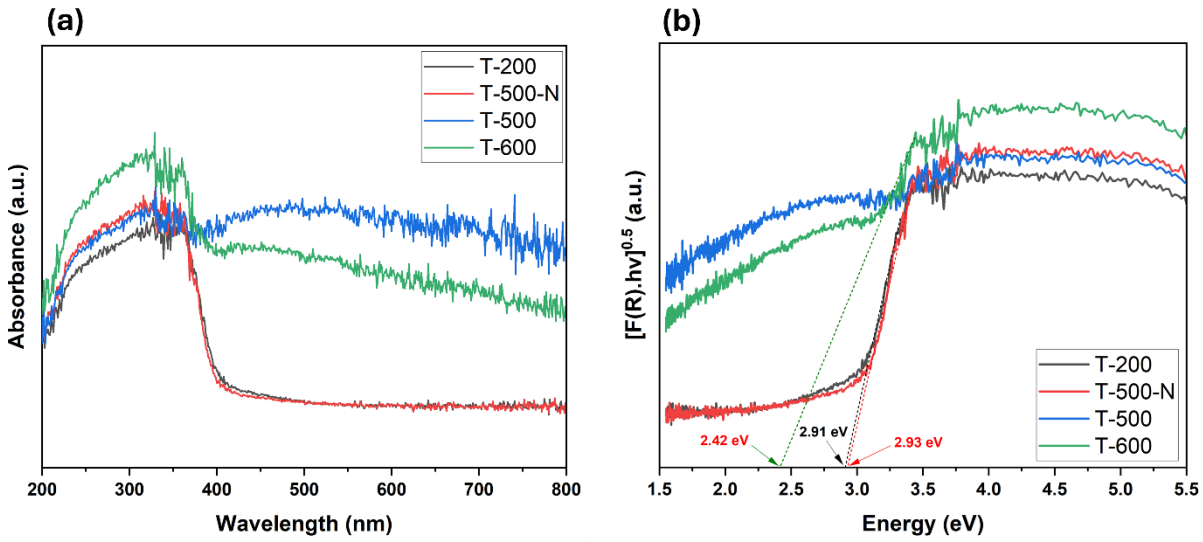

Figure 4 (a) UV-vis diffuse reflectance spectra and (b) Tauc plots of the synthesized TiO_2 samples.

Band gap energies were derived from the Tauc plots in Figure 4(b). The estimated band gaps for T-200, T-500-N, and T-600 were 2.91, 2.93, and 2.42 eV, respectively. The smaller effective band gap of T-600 compared with T-200 and T-500-N indicates that the reduced sample contained defect-related electronic states that extended the light absorption range. These states may appear as conduction-band tailing or intermediate levels within the TiO_2 band structure. For T-500, a clear band gap value could not be assigned because several overlapping features appeared in the Tauc plot. Such behavior is often found in doped, highly defective, or surface-modified semiconductors and may arise from interband states related to oxygen vacancies, Ti^{3+} centers, or residual surface species (J. Li et al., 2021).

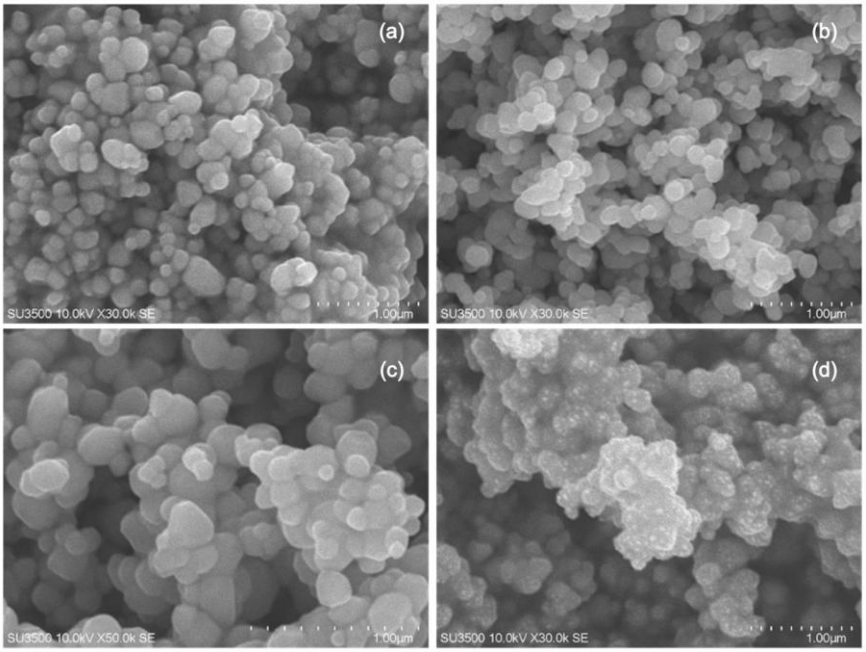

Figure 5 SEM images of the synthesized TiO_2 samples: (a) T-200, (b) T-500-N, (c) T-500, and (d) T-600.

The SEM images in Figure 5 show that all TiO_2 samples are composed of agglomerated particles with irregular, granular morphology. This aggregation is commonly observed for sol-gel-derived TiO_2 after calcination, as particle growth and interparticle contact occur during thermal treatment (Langa et al., 2023). Although BET surface area analysis was not performed in this study, the SEM observations provide qualitative information on particle aggregation and morphology. T-200 shows relatively fine and loosely packed aggregates (Figure 5(a)), which is consistent with its lower calcination temperature and smaller crystallite size observed from XRD (Figure 3(a)). The XRD result also showed lower crystallinity for T-200, indicating that limited thermal energy at 200 °C restricted crystal growth and particle coarsening. T-500-N, which was synthesized without $NaBH_4$ reduction, exhibits relatively uniform aggregates and a lighter morphology. Its white color and weak visible-light absorption in Figure 4 suggest that defect-related optical states were not significantly developed. The clearer Raman bands of T-500-N (Figure 3(b)) compared with T-500 also indicate a more ordered anatase lattice with fewer defect-induced distortions.

In contrast, T-500 shows larger and more compact agglomerates compared with T-200 and T-500-N. The darker appearance of this sample, together with its strong visible-light absorption in UV-vis DRS (Figure 4) and suppressed Raman peak intensity (Figure 3(b)), suggests the formation of a higher concentration of Ti^{3+} associated with oxygen vacancy-related defect states. These defects may contribute to lattice disorder and surface structural modification, which is reflected in the more compact and irregular morphology (Y. Xu et al., 2017). T-600 displays strongly aggregated particles with rougher and denser clusters. This morphology is consistent with the higher crystallinity and larger crystallite size obtained from XRD (Figure 3(a)), indicating thermally promoted crystal growth and sintering at higher calcination temperature. The dark brown color and enhanced visible-light absorption of T-600 further support the presence of defect states, while its stronger Raman peaks compared with T-500 suggest that improved crystallinity partly offsets the defect-induced disorder.

Photocatalytic Assessment

The photocatalytic degradation performance of T-200, T-500-N, T-500, and T-600 toward methylene blue is presented in Figure 6. The calibration curve in Figure 6(a) gave an R^2 value of 0.9990, confirming that UV-vis absorbance was linearly correlated with methylene blue concentration in the analyzed range. The degradation profiles in Figure 6(b) show clear differences in photocatalytic activity among the samples. T-200 exhibited negligible methylene blue degradation, with C_t/C_0 remaining close to 1 after 180 min irradiation. In contrast, T-500-N showed moderate activity, reducing C_t/C_0 to approximately 0.49. The $NaBH_4$-reduced samples showed significantly higher activity, with T-500 and T-600 decreasing C_t/C_0 to around 0.19 and 0.03, respectively.

DOI: 10.5614/j.eng.technol.sci.2026.58.5.10

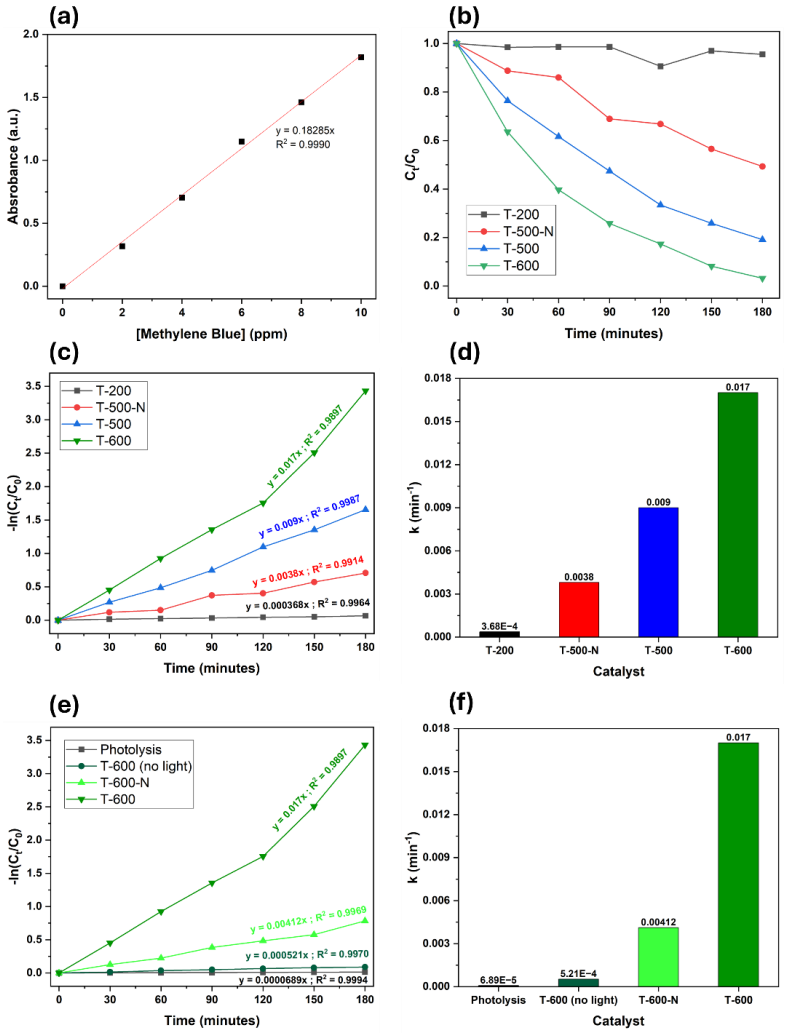

Figure 6 Photocatalytic degradation of methylene blue: (a) calibration curve, (b) C_t/C_0 profiles, (c) pseudo-first-order kinetic plots, and (d) apparent rate constants for T-200, T-500-N, T-500, and T-600. Control experiments for the optimized T-600 sample are shown as (e) pseudo-first-order kinetic plots and (f) apparent rate constants under photolysis, dark/no-light condition, non-reduced T-600-N, and photocatalytic T-600 conditions.

The kinetic plots were analyzed using the pseudo-first-order expression $-\ln(C_t/C_0) = kt$, as presented in Figure 6(c) **c**. This model was applied because methylene blue was used at low concentration and the catalyst loading and O_2 purging was kept constant, allowing the degradation rate to be approximated as a function of dye concentration. In this analysis, C_0 was defined as the initial methylene blue concentration before the dark adsorption step, while C_t represents the concentration at each irradiation time. The fitting quality was evaluated using the coefficient of determination (R^2), which has been added to the revised kinetic plots. The obtained R^2 values indicate acceptable linearity of the pseudo-first-order fitting, supporting its use for comparing the apparent degradation rates among the catalysts. The apparent rate constants obtained from the slopes are compared in Figure 6(d). T-600 showed the highest rate constant of 0.017 min^{-1}, followed by T-500 at 0.009 min^{-1}, T-500-N at 0.0038 min^{-1}, and T-200 at 3×10^{-4} min^{-1}. These results indicate that $NaBH_4$-assisted reduction greatly enhanced the photocatalytic performance of TiO_2, as shown by the higher activity of T-500 compared with the non-reduced T-500-N.

The additional control experiments in Figures 6(e)-(f) further confirm that the high activity of T-600 originated from the combined effect of light irradiation and the $NaBH_4$-reduced TiO_2 catalyst. Photolysis alone showed negligible degradation, while T-600 under dark conditions also gave a very low-rate constant, indicating that adsorption was not the main removal pathway. The non-reduced T-600 (T-600-N) exhibited only moderate activity, with a rate constant of 0.0042 min^{-1}, much lower than that of T-600. This confirms that the improved performance of T-600 was mainly caused by defect engineering through $NaBH_4$ reduction, which enhanced visible-light absorption and promoted photocatalytic degradation rather than simple dye adsorption or direct photolysis.

Although methylene blue is widely used as a model dye for photocatalytic evaluation, its use as the sole pollutant represents a limitation because methylene blue can be photosensitized under light irradiation. Therefore, the apparent degradation activity may not originate exclusively from the photocatalyst. In this work, the photolysis control experiment showed negligible degradation, suggesting that direct photolysis or photosensitization was not the main contributor under the applied conditions. Nevertheless, future studies should evaluate additional pollutants, preferably non-photosensitizing organic compounds, to further confirm the general applicability of the defect-engineered TiO_2 photocatalyst.

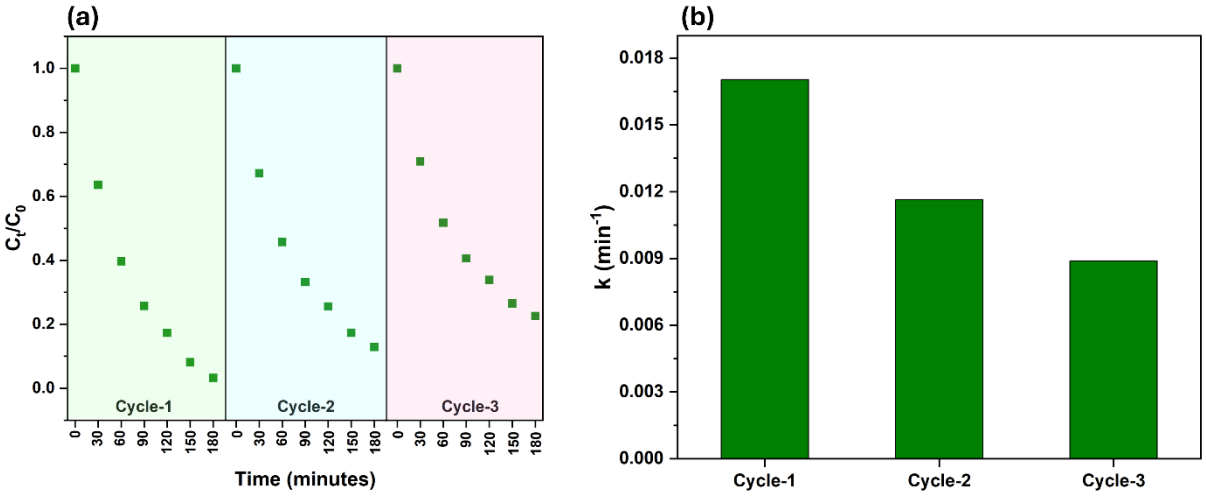

Figure 7 Photocatalytic stability test of the T-600 sample for methylene blue degradation over three consecutive cycles: (a) Ct/C_o profiles as a function of irradiation time and (b) apparent pseudo-first-order rate constants for each cycle.

The reusability of T-600 was evaluated for three consecutive photocatalytic cycles (Figure 7). The apparent rate constant decreased from 0.017 min^{-1} in the first cycle to 0.0116 and 0.0089 min^{-1} in the second and third cycles, respectively, indicating that T-600 retained photocatalytic activity after repeated use, although gradual deactivation occurred due to possible catalyst loss, surface fouling, or partial modification of defect-related active sites.

Discussion

The improved activity of T-500 and T-600 is consistent with the previous physicochemical characterization. UV-vis DRS showed that both samples had enhanced visible-light absorption, indicating the formation of defect-related energy states associated with Ti^{3+} species and oxygen vacancies. Raman analysis (Figure 3(b)) also suggested higher defect-related features in the reduced samples, particularly through changes in peak intensity and photoluminescence background. These defects can improve light harvesting and facilitate charge separation, thereby increasing the generation of reactive oxygen species during photocatalysis.

Although T-500 showed stronger visible-light absorption than T-600 (Figure 4), its photocatalytic activity was lower. This suggests that excessive defect formation may act as recombination centers or block active sites, reducing photocatalytic efficiency (Z. Li et al., 2022). T-600 appears to provide a more favorable compromise between defect concentration and crystal quality. The XRD results (Figure 3(a)) showed that calcination at 600 °C improved crystallinity and increased crystallite size, which can support charge transport and reduce bulk recombination. At the same time, sufficient defect states remained to broaden visible-light response. Therefore, the best activity of T-600 is assigned to the combined effect of anatase crystallinity, visible-light absorption, and an appropriate amount of Ti^{3+}-oxygen vacancy sites (Madima et al., 2025). Since the photocatalytic reaction was performed under the full Xe lamp spectrum without wavelength filtering, the enhanced activity of T-600 cannot be attributed solely to visible-light absorption. The stronger UV-region absorption of T-600, together with its sufficient visible-light response, higher crystallinity, and balanced defect states, likely contributed to its superior performance. In contrast, although T-500 showed stronger visible-light absorption, its lower crystallinity and possibly excessive defect density may have promoted charge recombination, leading to lower activity than T-600.

The rate constants summarized in Table 1 were obtained under different reaction conditions, including methylene blue concentration, catalyst loading, light source, irradiation wavelength, and reactor configuration. Therefore, direct comparison of rate constants is not appropriate because these parameters strongly influence the apparent degradation

DOI: 10.5614/j.eng.technol.sci.2026.58.5.10

rate. Instead, Table 1 is used as a general benchmark to position the present $NaBH_4$-reduced TiO_2 within the range of reported defective TiO_2-based photocatalysts. The T-600 sample delivered an apparent rate constant of 1.7×10^{-2} min^{-1} for methylene blue degradation. This value is higher than that reported for plasma-treated TiO_2 (7.0×10^{-3} min^{-1}) and comparable to some thermally treated defective TiO_2 systems. However, it is lower than those obtained using vacuum annealing, UV-assisted low-temperature annealing, sol-gel, solvothermal self-doping, and combination of solvothermal and chemical reduction approaches, which reported rate constants in the range of 3.6×10^{-2} to 1.3×10^{-1} min^{-1}. The lower activity in this work may be related to differences in reaction conditions, including the broader irradiation wavelength range, catalyst loading, MB concentration, and the extent of defect formation. Nevertheless, the present catalyst was prepared through a relatively simple chemical reduction route and still exhibited measurable photocatalytic activity, indicating that defect engineering through chemical reduction can effectively enhance the visible-light response of TiO_2 for dye degradation.

Table 1 Comparison of photocatalytic methylene blue degradation using defective TiO_2-based photocatalysts synthesized by different methods under various reaction conditions.

Synthesis method	MB concentration (mg/L)	Catalyst loading (g/L)	Light source	Reaction rate constant (k, min^{-1})	Reference
Hydrothermal	10.0	0.50	300 W Xenon, $\lambda > 420$ nm	2.0×10^{-2}	(Wajid Shah et al., 2015)
Plasma	10.0	n.a.	15 W UV-vis, λ = 300-1100 nm	7.0×10^{-3}	(Godoy Junior et al., 2020)
Vacuum annealing	10.0	0.25	500 W Hg lamp, $\lambda > 420$ nm	3.6×10^{-2}	(Chen, Xiao, et al., 2018)
UV and low temperature annealing	10.0	0.25	500 W Hg lamp, $\lambda > 420$ nm	4.6×10^{-2}	(Chen, Wang, et al., 2018)
Solvothermal	20.0	0.20	300 W Xenon, $\lambda > 420$ nm	1.3×10^{-1}	(Xin et al., 2015)
Sol-gel	10.0	0.07	300 W Xenon, $\lambda > 400$ nm	8.3×10^{-2}	(Wang et al., 2017)
Solvothermal, self-doped TiC_3	6.4	2.00	300 W Xenon, $\lambda > 420$ nm	7.1×10^{-2}	(Zhu et al., 2014)
Chemical reduction – $NaBH_4$	10	1.00	300 W Xenon, λ = 200-1000 nm	1.7×10^{-2}	This work

Proposed Mechanism

The proposed photocatalytic mechanism of methylene blue degradation over Ti^{3+} self-doped TiO_{2-x} is illustrated in Figure 7. When the catalyst is exposed to Xenon light, electrons are promoted from the valence band (VB) to the conduction band (CB), leaving holes in the VB. In defect-rich TiO2-x, Ti3+ sites and oxygen vacancies generate electronic states inside the band gap. These states can broaden optical absorption toward the visible region and can temporarily trap photoexcited electrons, thereby supporting charge separation. This interpretation is consistent with the UV-vis DRS data in Figure 4, where T-500 and T-600 absorbed visible light more strongly than T-200 and T-500-N. It also agrees with the Raman spectra in Figure 3(b), which showed defect-related lattice disorder in the reduced samples. The color change from white to black or dark brown shown in Figure 2 further confirms that $NaBH_4$ treatment altered the electronic structure of TiO_2 through Ti^{3+}-oxygen vacancy formation.

Following photoexcitation, electrons located in the CB or defect states can reduce dissolved O_2 to form superoxide radicals ($O_2\bullet^-$). Simultaneously, holes remaining in the VB can oxidize H_2O or OH^- to generate hydroxyl radicals (•OH). These reactive oxygen species, together with photogenerated holes, attack methylene blue molecules and convert them into less colored intermediates and, ultimately, mineralized products such as CO_2 and H_2O. On this basis, the superior activity of T-600 is attributed to the simultaneous presence of improved anatase crystallinity, extended visible-light

absorption, and a suitable density of Ti^{3+}-oxygen vacancy defect sites that favor charge separation and reactive oxygen species formation (Z. Li et al., 2022).

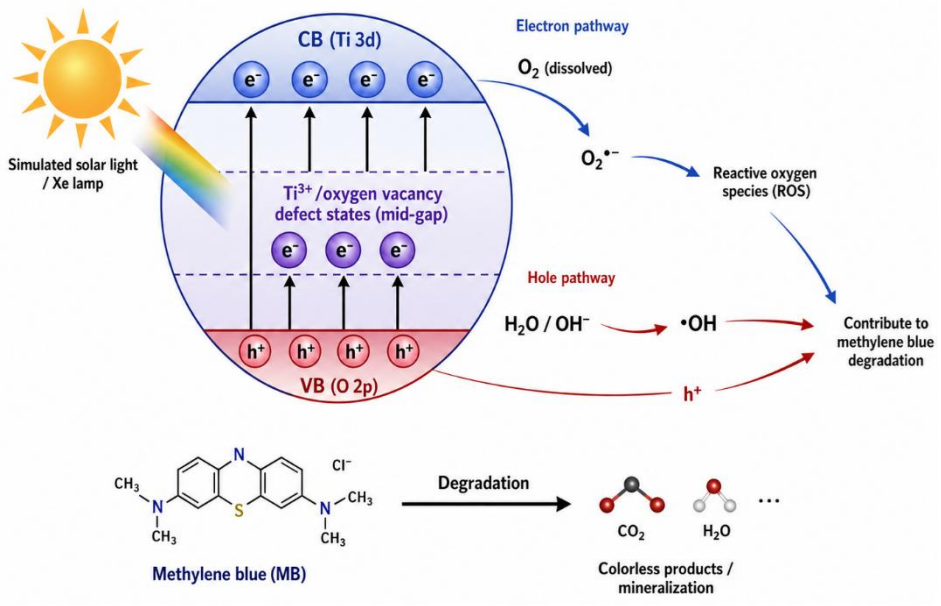

Figure 8 Proposed photocatalytic mechanism of methylene blue degradation over Ti^{3+} self-doped TiO_{2-x} under Xenon light irradiation

Conclusion

Ti^{3+} self-doped TiO_2 photocatalysts were successfully prepared through a $NaBH_4$-assisted sol-gel calcination route. Both the reduction step and calcination temperature affected the structural, optical, defect, morphological, and photocatalytic characteristics of the materials. XRD confirmed that the selected samples retained the anatase phase, while higher calcination temperature increased crystallinity and crystallite size. Raman spectroscopy supported the anatase assignment and indicated defect-related lattice disorder in the reduced samples. EPR analysis directly confirmed the formation of Ti^{3+}/oxygen-vacancy defect sites, with T-600 showing the strongest defect signal. UV-vis DRS showed that $NaBH_4$ treatment enhanced visible-light absorption, particularly for T-500 and T-600, whereas SEM observations revealed stronger aggregation and rougher morphology at higher calcination temperature. Photocatalytic testing demonstrated that $NaBH_4$-assisted reduction and high-temperature calcination significantly improved methylene blue degradation. T-200 was nearly inactive, T-500-N showed moderate performance, and the reduced samples T-500 and T-600 exhibited much higher activity with apparent pseudo-first-order rate constants of 0.009 and 0.017 min^{-1}, respectively. Control experiments confirmed that the superior activity of T-600 resulted from the combined effect of light irradiation and the $NaBH_4$-reduced TiO_2 catalyst, rather than direct photolysis or dye adsorption. The non-reduced T-600-N showed much lower activity, highlighting the important role of defect engineering. The stability test further showed that T-600 retained photocatalytic activity over three consecutive cycles, although the rate constant gradually decreased from 0.017 to 0.0116 and 0.0089 min^{-1} due to possible catalyst loss, surface fouling, or partial modification of defect-related active sites. The highest activity of T-600 is explained by the balanced contribution of enhanced anatase crystallinity, improved visible-light harvesting, and an appropriate amount of Ti^{3+}-oxygen vacancy defects. In comparison, the lower activity of T-500 despite stronger visible absorption indicates that excessive defects may increase recombination or limit available active sites. Ultimately, this work confirms that controlled $NaBH_4$-assisted defect engineering is an effective strategy for improving anatase TiO_2 photocatalysts for methylene blue degradation, and highlights calcination temperature as a key parameter for balancing anatase crystallinity, visible-light absorption, and Ti^{3+}-oxygen vacancy defect formation.

Acknowledgement

This research was funded by Reguler Fundamental Research Program from the Ministry of Higher Education, Science, and Technology, Republic of Indonesia 2025 (Grant No. 349.IT1.B07.1/SPP-DRI/V/2025).

DOI: 10.5614/j.eng.technol.sci.2026.58.5.10

Compliance with ethics guidelines

The authors declare they have no conflict of interest or financial conflicts to disclose.

This article contains no studies with human or animal subjects performed by the authors.

References

Abdullah, S. A., Sahdan, M. Z., Nayan, N., Embong, Z., Hak, C. R. C., & Adriyanto, F. (2020). Neutron beam interaction with rutile TiO2 single crystal (1 1 1): Raman and XPS study on Ti3+-oxygen vacancy formation. *Materials Letters*, *263*, 127143. https://doi.org/https://doi.org/10.1016/j.matlet.2019.127143

Bharti, B., Kumar, S., Lee, H.-N., & Kumar, R. (2016). Formation of oxygen vacancies and Ti3+ state in TiO2 thin film and enhanced optical properties by air plasma treatment. *Scientific Reports*, *6*(1), 32355. https://doi.org/10.1038/srep32355

Chen, S., Wang, Y., Li, J., Hu, Z., Zhao, H., Xie, W., & Wei, Z. (2018). Synthesis of black TiO2 with efficient visible-light photocatalytic activity by ultraviolet light irradiation and low temperature annealing. *Materials Research Bulletin*, *98*, 280–287. https://doi.org/https://doi.org/10.1016/j.materresbull.2017.10.036

Chen, S., Xiao, Y., Wang, Y., Hu, Z., Zhao, H., & Xie, W. (2018). A Facile Approach to Prepare Black TiO2 with Oxygen Vacancy for Enhancing Photocatalytic Activity. *Nanomaterials*, *8*(4). https://doi.org/10.3390/nano8040245

Deng, Y., & Zhao, R. (2015). Advanced Oxidation Processes (AOPs) in Wastewater Treatment. *Current Pollution Reports*, *1*(3), 167–176. https://doi.org/10.1007/s40726-015-0015-z

Fang, W., Xing, M., & Zhang, J. (2014). A new approach to prepare Ti3+ self-doped TiO2 via $NaBH_4$ reduction and hydrochloric acid treatment. *Applied Catalysis B: Environmental*, *160–161*, 240–246. https://doi.org/https://doi.org/10.1016/j.apcatb.2014.05.031

Gao, Q., Si, F., Zhang, S., Fang, Y., Chen, X., & Yang, S. (2019). Hydrogenated F-doped TiO2 for photocatalytic hydrogen evolution and pollutant degradation. *International Journal of Hydrogen Energy*, *44*(16), 8011–8019. https://doi.org/https://doi.org/10.1016/j.ijhydene.2019.01.233

Godoy Junior, A., Pereira, A., Gomes, M., Fraga, M., Pessoa, R., Leite, D., Petraconi, G., Nogueira, A., Wender, H., Miyakawa, W., Massi, M., & da Silva Sobrinho, A. (2020). Black TiO2 Thin Films Production Using Hollow Cathode Hydrogen Plasma Treatment: Synthesis, Material Characteristics and Photocatalytic Activity. *Catalysts*, *10*(3). https://doi.org/10.3390/catal10030282

Guillemot, F., Porté, M. C., Labrugère, C., & Baquey, C. (2002). Ti4+ to Ti3+ Conversion of TiO2 Uppermost Layer by Low-Temperature Vacuum Annealing: Interest for Titanium Biomedical Applications. *Journal of Colloid and Interface Science*, *255*(1), 75–78. https://doi.org/https://doi.org/10.1006/jcis.2002.8623

Hamdy, M. S., Saputera, W. H., Groenen, E. J., & Mul, G. (2014). A novel TiO2 composite for photocatalytic wastewater treatment. *Journal of Catalysis*, *310*, 75–83. https://doi.org/https://doi.org/10.1016/j.jcat.2013.07.017

Jiménez, J. M., Zickler, G. A., Redhammer, G. J., & Berger, T. (2023). Chemical reduction of porous WO3 and TiO2 photoelectrocatalysts by atomic hydrogen. *Applied Catalysis A: General*, *658*, 119163. https://doi.org/https://doi.org/10.1016/j.apcata.2023.119163

Langa, C., Tetana, Z. N., & Hintsho-Mbita, N. C. (2023). Effect of calcination temperature on the synthesis of TiO2 nanoparticles from Sutherlandia frutescence for the degradation of Congo red dye and antibiotics ciproflaxin and sulfamethoxazole. *Chemical Physics Impact*, *7*, 100389. https://doi.org/https://doi.org/10.1016/j.chphi.2023.100389

Lee, J., Li, Z., Zhu, L., Xie, S., & Cui, X. (2018). Ti3+ self-doped TiO2 via facile catalytic reduction over Al(acac)3 with enhanced photoelectrochemical and photocatalytic activities. *Applied Catalysis B: Environmental*, *224*, 715–724. https://doi.org/https://doi.org/10.1016/j.apcatb.2017.10.057

Li, J., Cheng, D., Chen, Z., Yang, L., Zheng, L., Wei, Z., Ma, T., Zhang, J., & Luo, Y. (2021). Oxygen vacancy/Ti3+ engineered TiO2 nanotube arrays prepared by in-situ exfoliation with H2 bubbles: A visible-light-driven self-supporting photocatalyst for detoxfication of chloraphenicol. *Journal of Environmental Chemical Engineering*, *9*(6), 106670. https://doi.org/https://doi.org/10.1016/j.jece.2021.106670

Li, Z., Wang, S., Wu, J., & Zhou, W. (2022). Recent progress in defective TiO2 photocatalysts for energy and environmental applications. *Renewable and Sustainable Energy Reviews*, *156*, 111980. https://doi.org/https://doi.org/10.1016/j.rser.2021.111980

Madima, N., Chauke, N. M., Ngqoloda, S., Mmelesi, O. K., & Raphulu, M. (2025). Recent advances in the development of defective black TiO2 nanomaterials for application in energy and environmental sustainability: A review. *Results in Engineering*, *26*, 104868. https://doi.org/https://doi.org/10.1016/j.rineng.2025.104868

Ren, R., Wen, Z., Cui, S., Hou, Y., Guo, X., & Chen, J. (2015). Controllable Synthesis and Tunable Photocatalytic Properties of Ti3+-doped TiO2. *Scientific Reports*, *5*(1), 10714. https://doi.org/10.1038/srep10714

Saputera, W. H., Amri, A. F., Mukti, R. R., Suendo, V., Devianto, H., & Sasongko, D. (2021). Photocatalytic Degradation of Palm Oil Mill Effluent (POME) Waste Using BiVO4 Based Catalysts. *Molecules*, *26*(20). https://doi.org/10.3390/molecules26206225

Saputera, W. H., Mul, G., & Hamdy, M. S. (2015). Ti3+-containing titania: Synthesis tactics and photocatalytic performance. *Catalysis Today*, *246*, 60–66. https://doi.org/https://doi.org/10.1016/j.cattod.2014.07.049

Saputera, W. H., Pranata, J. J., Jonatan, R., Widiatmoko, P., & Sasongko, D. (2023). Photocatalytic Simulation of Phenol Waste Degradation Using Titanium Dioxide (TiO2) P25-Based Photocatalysts. *Journal of Engineering and Technological Sciences*, *55*(4), 419–433. https://doi.org/10.5614/j.eng.technol.sci.2023.55.4.6

Saputera, W. H., Sasongko, D., Widiatmoko, P., Yatasha Dewi, N., & Ardhistira, A. M. (2024). Simulation of photocatalytic degradation of methylene blue using titanium dioxide (TiO2) P25 as a photocatalyst. *AIP Conference Proceedings*, *3073*(1), 080006. https://doi.org/10.1063/5.0194112

Shindhal, T., Rakholiya, P., Varjani, S., Pandey, A., Ngo, H. H., Guo, W., Ng, H. Y., & Taherzadeh, M. J. (2021). A critical review on advances in the practices and perspectives for the treatment of dye industry wastewater. *Bioengineered*, *12*(1), 70–87. https://doi.org/10.1080/21655979.2020.1863034

Ullattil, S. G., & Ramakrishnan, R. M. (2018). Defect-Rich Brown TiO2–x Porous Flower Aggregates: Selective Photocatalytic Reversibility for Organic Dye Degradation. *ACS Applied Nano Materials*, *1*(8), 4045–4052. https://doi.org/10.1021/acsanm.8b00824

Wajid Shah, M., Zhu, Y., Fan, X., Zhao, J., Li, Y., Asim, S., & Wang, C. (2015). Facile Synthesis of Defective TiO2−x Nanocrystals with High Surface Area and Tailoring Bandgap for Visible-light Photocatalysis. *Scientific Reports*, *5*(1), 15804. https://doi.org/10.1038/srep15804

Wang, T., Li, W., Xu, D., Wu, X., Cao, L., & Meng, J. (2017). Strong visible absorption and excellent photocatalytic performance of brown TiO2 nanoparticles synthesized using one-step low-temperature process. *Chinese Journal of Catalysis*, *38*(7), 1184–1195. https://doi.org/https://doi.org/10.1016/S1872-2067(17)62855-9

Xin, X., Xu, T., Yin, J., Wang, L., & Wang, C. (2015). Management on the location and concentration of Ti3+ in anatase TiO2 for defects-induced visible-light photocatalysis. *Applied Catalysis B: Environmental*, *176–177*, 354–362. https://doi.org/https://doi.org/10.1016/j.apcatb.2015.04.016

Xu, C., Rangaiah, G. P., & Zhao, X. S. (2014). Photocatalytic Degradation of Methylene Blue by Titanium Dioxide: Experimental and Modeling Study. *Industrial & Engineering Chemistry Research*, *53*(38), 14641–14649. https://doi.org/10.1021/ie502367x

Xu, Y., Wu, S., Wan, P., Sun, J., & Hood, Z. D. (2017). Introducing Ti3+ defects based on lattice distortion for enhanced visible light photoreactivity in TiO2 microspheres. *RSC Advances*, *7*(52), 32461–32467. https://doi.org/10.1039/C7RA04885H

Zhu, Q., Peng, Y., Lin, L., Fan, C.-M., Gao, G.-Q., Wang, R.-X., & Xu, A.-W. (2014). Stable blue TiO2−x nanoparticles for efficient visible light photocatalysts. *Journal of Materials Chemistry A*, *2*(12), 4429–4437. https://doi.org/10.1039/C3TA14484D

Zywitzki, D., Jing, H., Tüysüz, H., & Chan, C. K. (2017). High surface area, amorphous titania with reactive Ti3+ through a photo-assisted synthesis method for photocatalytic H2 generation. *Journal of Materials Chemistry A*, *5*(22), 10957–10967. https://doi.org/10.1039/C7TA01614J

Manuscript Received: May 6th, 2026
Revised Manuscript Revision Received: 2 July 2026
Accepted Manuscript: 22 July 2026